

Appendix A

Fountain Beam Deflection Due to Electric Field Plate Misalignment

If the electric field plates (atoms travel in the vertical z direction, and the electric field is in the y direction) have a gap spacing narrower at one end (in the x direction) than the other, the resulting electric field gradient (See Eq. A.1) will deflect the atoms towards the narrow side, leading to a possible loss of signal.

In all atoms, an electric field $E = (E_x^2 + E_y^2 + E_z^2)^{1/2}$ induces a non-permanent electric dipole moment in the atom. The induced dipole moment in turn interacts with the electric field leading to an interaction energy W , where $W = -\frac{1}{2}\alpha E^2$ and where for francium in its ground state $\alpha = 5.3 \times 10^{-39} \text{ J m}^2 \text{ V}^{-2} = 8.0 \times 10^{-6} \text{ Hz m}^2 \text{ V}^{-2}$ is the static dipole polarizability [SJD99].

In an inhomogeneous electric field, the atom undergoes an acceleration a towards the stronger electric field (is strong-field seeking). The acceleration toward the narrow side is

$$a_x = -\frac{1}{m} \frac{\partial W}{\partial x} = -\frac{1}{m} \frac{\partial W}{\partial E} \frac{\partial E}{\partial x} = \frac{\alpha}{m} E \frac{\partial E}{\partial x}, \quad (\text{A.1})$$

where $m = 3.5 \times 10^{-25} \text{ kg}$ is the mass of ^{211}Fr .

For a cesium fountain scalar polarizability measurement, done by measuring the travel time in a fountain as a function of electric field [AG03], the electric field plates had a random variation in gap spacing of up to 4 microns. Those plates were machined from aluminum with the gap spacing determined by alumina spacers. The only attempts to maintain uniformity were that all of the spacers were ground simultaneously, and that the two electric field plates were milled (using an ordinary milling machine) in

the same fixture. No attempt was made to achieve a precisely set gap spacing. We therefore assume for this calculation that carefully fabricated and assembled electric field plates for the EDM experiment will do no worse.

To model the deflection of a francium fountain due to variation in the gap spacing, a model set of 300 mm-long by 50 mm-wide electric field plates is divided into ten sections as shown in Fig. A.1 with five sections on each side of the vertical centerline. Each of the ten sections can have a gap spacing that deviates from the 5 mm half-gap spacing by up to ± 2 microns, and each of the ten sections is 50 mm high by 20 mm wide, leaving a 10 mm border between sections. This border region is maintained at the nominal gap spacing. Electric field gradients

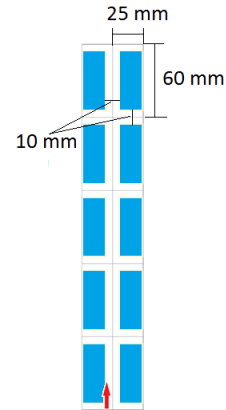


Figure A.1: Model electric field plates showing the regions with random variations in gap spacing in blue.

are produced between a border region and one of the ten sections, or between two sections. The nominal electric field $E = E_y$ is 10^7 V/m and the velocity of the francium atoms entering the electric field plates¹ is 2.3 m/s. We neglect end effects.

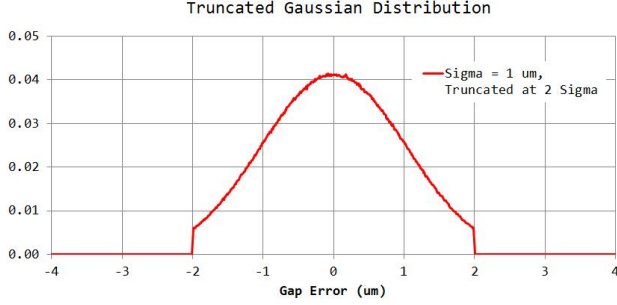


Figure A.2: Probability distribution of gap spacing variations. The average is zero, the RMS is ± 1 micron and is truncated at ± 2 microns.

Each of the ten regions is assigned a gap variation that follows a truncated Gaussian probability distribution shown in Fig. A.2. Once each of the ten regions has been assigned a gap variation, the electric fields in the areas between regions is determined by a linear interpolation. Atoms traveling in the center 10 mm between the two sets of five regions will experience the resulting gradient and be deflected (Fig. A.3). In this model, atoms outside the ± 5 mm center section will not experience a gradient: however our beam transport solution keeps the francium atoms to within 4 mm of the axis in the main electric field plates (Fig. 3.24).

The atoms enter the electric field region traveling in the vertical z direction. Twenty one trajectories are followed with initial horizontal positions x_i ranging from $x_i = -10$ mm to $x_i = +10$ mm in 1 mm steps, as shown in Fig. A.3. We used 200 different random trials and the mesh size is 0.1 mm to make a space of 500×3000 .

An example of the trajectories from one of the 200 trials is shown in Fig. A.3. The displacements are relatively uniform over $-5 \text{ mm} < x_i < 5 \text{ mm}$.

¹They will have slowed down from ≈ 3 m/s in the electrostatic focusing triplet.

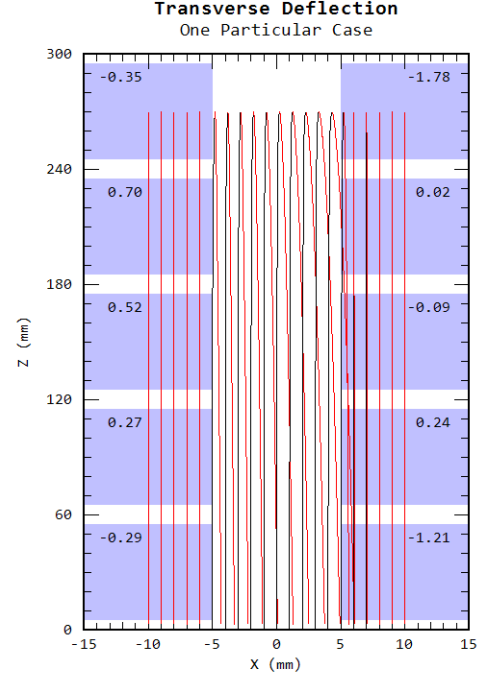


Figure A.3: Trajectory example: atoms launched at $x_i = -10, -9, -8, \dots, 0, \dots, 8, 9, 10$ mm, and returning after deflection.

A tally of the deflection from 200 trials is shown in Fig. A.4. Shown is the magnitude of the average deflection (red) and RMS deflection (blue) as a function of the initial horizontal position of the beam. **Deflection of the beam appears limited to 1 mm or less.**

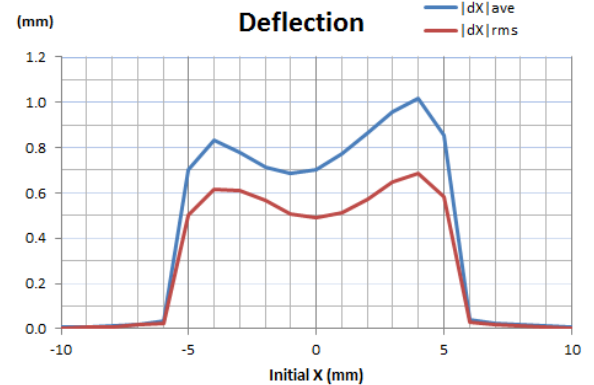


Figure A.4: Magnitude of the average deflection and RMS deflection as a function of fountain position.

Appendix B

Appendix to Chapter 5 – Motional Systematic Effects

B.1 Detection by Fluorescence

The scheme for detecting the ratio of ^{211}Fr atoms that remain in the $7S_{1/2}$, $F = 5$ hyperfine level to the total number of atoms by the counting of scattered photons has some subtleties, which we delve into here.

The first subtlety is that it is desirable to have the fluorescence laser (that is tuned to the transition $7S_{1/2}$, $F = 5 \rightarrow 7P_{3/2}$, $F' = 6$) be circularly polarized [AMG07]. Were it linearly polarized, the laser would catch the tails of the Lorentz profile of the off-resonant transitions $7S_{1/2}$, $F = 5 \rightarrow 7P_{3/2}$, $F' = 5$ and $7S_{1/2}$, $F = 5 \rightarrow 7P_{3/2}$, $F' = 4$; because both the $7P_{3/2}$, $F' = 5$ and $7P_{3/2}$, $F' = 4$ levels have a branch to the lower ground-state hyperfine level $7S_{1/2}$, $F = 4$, over many cycles of excitation and de-excitation the initial population in the upper ground-state hyperfine level would bleed into the lower. However if the laser is circularly polarized all the atoms swiftly settle into the cycling transition $7S_{1/2} |55\rangle \rightarrow 7P_{3/2} |66\rangle$; and the matrix element connecting the state $7S_{1/2} |55\rangle$ to any other $7P$ state is zero.

Any detector of a scattered photon will have an efficiency that will depend upon the direction of the photon and its polarization. The distribution of directions and polarization will depend somewhat on the states an atom in the $F = 5$ level will be in, until the atom settles into the cycling transition. It

is therefore desirable to gate off the photon detector until the atom so settles. It is also desirable to use a spherical mirror to collect photons that are directed away from the detector, both to maximize collection efficiency and to smooth out variations in the detection efficiency with the position of the atom.

To avoid having net momentum transferred to the atom from the laser beam, the fluorescing laser must be retroreflected. An atom is then as likely to absorb a photon traveling left as one traveling right, and so the average recoil velocity imparted to the atom for each photon scattered will be zero. Nonetheless atoms will acquire a distribution of velocities parallel to the laser axis with a finite root-mean-square value, whose effects we seek to minimize. Let ν_0 be the resonance frequency of the transition, and let ν be the frequency shift for some individual atom due to its velocity parallel to the beam, so that the frequency of the laser as seen in the atomic rest frame is $\nu_l + \nu$, where ν_l is the frequency of the laser as seen in the lab. Then the rate of photon scatter in a retroreflected laser will be

$$f \equiv \frac{1}{2} \left[\frac{\nu_w^2}{(\nu_0 - \nu_l - \nu)^2 + \nu_w^2} + \frac{\nu_w^2}{(\nu_0 - \nu_l + \nu)^2 + \nu_w^2} \right], \quad (\text{B.1})$$

where ν_w is (in cycles/s) the full-width at half-maximum of the Lorentz lineshape. We note ν enters with different signs in the two denominators; and that we have scaled so that $f = 1$ when $\nu = 0$ and $\nu_l = \nu_0$.

We note that f is an even function of ν and so an

expansion in powers of ν contains even powers only. If we tune the laser either above or below resonance, so that

$$|\nu_0 - \nu_l| = \frac{\nu_w}{\sqrt{3}}, \quad (\text{B.2})$$

then we can zero the coefficient of the term in f of order ν^2 , so that

$$f \rightarrow \frac{3}{4} + \frac{27}{64} \left(\frac{\nu}{\nu_w} \right)^4 + O(\nu)^6. \quad (\text{B.3})$$

This result may be compared to the result when we naïvely tune the laser on resonance, setting $\nu_0 - \nu_l = 0$, when we have instead

$$f \rightarrow 1 - \left(\frac{\nu}{\nu_w} \right)^2 + \left(\frac{\nu}{\nu_w} \right)^4 + O(\nu)^6. \quad (\text{B.4})$$

We see that tuning the laser off-resonance costs only 25% of the scattered photons (for a given power per unit area available from the laser), while it greatly suppresses changes to the fluorescence rate as a function of the Doppler shift when $\nu \ll \nu_w$. In practice the drop in the fluorescence rate after $\sim 10^4$ photon scatters is $\sim 1\%$ for a retroreflected laser running on resonance, and is a negligible $\sim 0.01\%$ for a laser running $\nu_w/\sqrt{3}$ either above or below resonance. Running below resonance is preferred to running above resonance, because the net atomic velocity parallel to the laser beam stabilizes to a sufficiently small value even if the intensities in the nominally equal primary and retroreflected beams differ slightly, and because the beam heating in the direction of the laser becomes limited by Doppler cooling.

B.2 Expansion of U_{up}

The Taylor expansion in powers of τ for U_{up} has been reported with errors $O(\tau^2)$ in Eq. (5.46). The expansion with the smaller error of $O(\tau^4)$ is

$$\begin{aligned} U_{\text{up}} = & 1 + \left(-\frac{1}{6} i c \epsilon \tau \right) X \\ & + \left(-\frac{1}{72} c^2 \epsilon^2 \tau^2 \right) XX \\ & + \left(+\frac{1}{1296} i \tau^3 c^3 \epsilon^3 \right) XXX \\ & + \left(-\frac{7}{1620} i c^2 \epsilon^2 \tau^3 y_0 - \frac{5}{648} i x_0 c \epsilon \tau^3 y_0 \right) XXY \end{aligned}$$

$$\begin{aligned} & + \left(-\frac{7}{1620} i c^2 \epsilon^2 \tau^3 z_0 - \frac{5}{648} i x_0 c \epsilon \tau^3 z_0 \right) XXZ \\ & + \left(+\frac{1}{810} i \tau^3 x_0^2 \epsilon^2 \right. \\ & \quad \left. - \frac{1}{3240} i \tau^3 x_0 c \epsilon^3 - \frac{1}{2835} i \tau^3 c^2 \epsilon^4 \right) XXXZ \\ & + \left(+\frac{1}{18} c \epsilon \tau^2 y_0 - \frac{5}{648} c \epsilon \tau^3 y_1 \right) XY \\ & + \left(-\frac{1}{1620} i \tau^3 c^2 \epsilon^2 y_0 + \frac{5}{324} i \tau^3 x_0 c \epsilon y_0 \right) XYX \\ & + \left(+\frac{5}{648} i \tau^3 c \epsilon y_0^2 \right) XYY \\ & + \left(+\frac{5}{648} i \tau^3 c \epsilon y_0 z_0 \right) XYZ \\ & + \left(-\frac{1}{648} i \tau^3 c \epsilon^3 y_0 + \frac{1}{810} i \tau^3 x_0 y_0 \epsilon^2 \right) XYZZ \\ & + \left(+\frac{1}{18} c \epsilon \tau^2 z_0 - \frac{5}{648} c \epsilon \tau^3 z_1 \right) XZ \\ & + \left(-\frac{1}{1620} i \tau^3 c^2 \epsilon^2 z_0 + \frac{5}{324} i \tau^3 x_0 c \epsilon z_0 \right) XZX \\ & + \left(+\frac{5}{648} i \tau^3 c \epsilon y_0 z_0 \right) XZY \\ & + \left(-\frac{1}{90} c \epsilon^3 \tau^2 - \frac{1}{36} x_0 \epsilon^2 \tau^2 \right. \\ & \quad \left. + \frac{1}{810} x_1 \epsilon^2 \tau^3 + \frac{5}{648} i \tau^3 c \epsilon z_0^2 \right) XZZ \\ & + \left(+\frac{29}{11340} i \tau^3 c^2 \epsilon^4 \right. \\ & \quad \left. + \frac{17}{3240} i c \epsilon^3 \tau^3 x_0 - \frac{1}{405} i x_0^2 \epsilon^2 \tau^3 \right) XZZX \\ & + \left(+\frac{1}{3240} i c \epsilon^3 \tau^3 y_0 - \frac{1}{405} i x_0 \epsilon^2 \tau^3 y_0 \right) XZZY \\ & + \left(-\frac{1}{810} i \tau^3 x_0 \epsilon^2 z_0 - \frac{1}{810} i \tau^3 c \epsilon^3 z_0 \right) XZZZ \\ & + \left(+\frac{1}{1296} i \tau^3 c \epsilon^5 + \frac{1}{567} i \tau^3 x_0 \epsilon^4 \right) XZZZZ \\ & + \left(-\frac{1}{18} c \epsilon \tau^2 y_0 + \frac{5}{648} c \epsilon \tau^3 y_1 \right) YX \\ & + \left(+\frac{2}{405} i \tau^3 c^2 \epsilon^2 y_0 - \frac{5}{648} i x_0 c \epsilon \tau^3 y_0 \right) YXX \\ & + \left(-\frac{5}{324} i c \epsilon \tau^3 y_0^2 \right) YXY \\ & + \left(-\frac{5}{324} i c \epsilon \tau^3 y_0 z_0 \right) YXZ \\ & + \left(+\frac{1}{810} i \tau^3 c \epsilon^3 y_0 + \frac{1}{810} i \tau^3 x_0 y_0 \epsilon^2 \right) YXZZ \\ & + \left(+\frac{5}{648} i \tau^3 c \epsilon y_0^2 \right) YYX \\ & + \left(+\frac{1}{810} i y_0^2 \epsilon^2 \tau^3 \right) YYZZ \\ & + \left(+\frac{5}{648} i \tau^3 c \epsilon y_0 z_0 \right) YZX \\ & + \left(-\frac{1}{36} y_0 \epsilon^2 \tau^2 + \frac{1}{810} y_1 \epsilon^2 \tau^3 \right) YZZ \\ & + \left(+\frac{2}{405} i \tau^3 c \epsilon^3 y_0 - \frac{1}{405} i x_0 \epsilon^2 \tau^3 y_0 \right) YZZX \\ & + \left(-\frac{1}{405} i y_0^2 \epsilon^2 \tau^3 \right) YZZY \\ & + \left(-\frac{1}{810} i y_0 \epsilon^2 \tau^3 z_0 \right) YZZZ \\ & + \left(+\frac{1}{567} i y_0 \epsilon^4 \tau^3 \right) YZZZZ \\ & + \left(-\frac{1}{18} c \epsilon \tau^2 z_0 + \frac{5}{648} c \epsilon \tau^3 z_1 \right) ZX \\ & + \left(+\frac{2}{405} i \tau^3 c^2 \epsilon^2 z_0 - \frac{5}{648} i x_0 c \epsilon \tau^3 z_0 \right) ZXX \\ & + \left(-\frac{5}{324} i c \epsilon \tau^3 y_0 z_0 \right) ZXY \\ & + \left(-\frac{5}{324} i c \epsilon \tau^3 z_0^2 \right) ZXZ \\ & + \left(+\frac{1}{810} i \tau^3 c \epsilon^3 z_0 + \frac{1}{810} i \tau^3 x_0 \epsilon^2 z_0 \right) ZXZZ \\ & + \left(+\frac{5}{648} i \tau^3 c \epsilon y_0 z_0 \right) ZYX \\ & + \left(+\frac{1}{810} i y_0 \tau^3 z_0 \epsilon^2 \right) ZYZZ \\ & + \left(+\frac{1}{90} c \epsilon^3 \tau^2 + \frac{1}{36} x_0 \epsilon^2 \tau^2 \right. \\ & \quad \left. - \frac{1}{810} x_1 \epsilon^2 \tau^3 + \frac{5}{648} i \tau^3 c \epsilon z_0^2 \right) ZZX \end{aligned}$$

$$\begin{aligned}
& + \left(-\frac{5}{2268} i\tau^3 c^2 \epsilon^4 \right. \\
& \quad \left. - \frac{2}{405} i c \epsilon^3 \tau^3 x_0 + \frac{1}{810} i \tau^3 x_0^2 \epsilon^2 \right) ZZX X \\
& + \left(+\frac{1}{810} i \tau^3 c \epsilon^3 y_0 + \frac{1}{810} i \tau^3 x_0 y_0 \epsilon^2 \right) ZZX Y \\
& + \left(+\frac{1}{810} i \tau^3 c \epsilon^3 z_0 + \frac{1}{810} i \tau^3 x_0 \epsilon^2 z_0 \right) ZZX Z \\
& + \left(-\frac{1}{648} i \tau^3 c \epsilon^5 - \frac{2}{567} i \tau^3 x_0 \epsilon^4 \right) ZZX ZZ \\
& + \left(+\frac{1}{36} y_0 \epsilon^2 \tau^2 - \frac{1}{810} y_1 \epsilon^2 \tau^3 \right) ZZ Y \\
& + \left(+\frac{1}{810} i \tau^3 x_0 y_0 \epsilon^2 - \frac{1}{162} i \tau^3 c \epsilon^3 y_0 \right) ZZ Y X \\
& + \left(+\frac{1}{810} i y_0^2 \epsilon^2 \tau^3 \right) ZZ Y Y \\
& + \left(+\frac{1}{810} i y_0 \tau^3 z_0 \epsilon^2 \right) ZZ Y Z \\
& + \left(-\frac{2}{567} i y_0 \tau^3 \epsilon^4 \right) ZZ Y ZZ \\
& + \left(-\frac{1}{810} i \tau^3 x_0 \epsilon^2 z_0 - \frac{1}{810} i \tau^3 c \epsilon^3 z_0 \right) ZZZ X \\
& + \left(-\frac{1}{810} i y_0 \epsilon^2 \tau^3 z_0 \right) ZZZ Y \\
& + \left(+\frac{1}{1296} i \tau^3 c \epsilon^5 + \frac{1}{567} i \tau^3 x_0 \epsilon^4 \right) ZZZ X X \\
& + \left(+\frac{1}{567} i y_0 \epsilon^4 \tau^3 \right) ZZZ X Y
\end{aligned} \tag{B.5}$$

Here x_n represents the n^{th} derivative with respect to t of the x -component of the static magnetic field evaluated at the point the atom hits the location of the effective step in the electric field; a similar convention holds for the y and z components of the static field. Here for typographic convenience we use the notation $X = \mathbf{F}_x$ and $Y = \mathbf{F}_y$ and $Z = \mathbf{F}_z$.

B.3 Values of the Constants c_{jn}

The following are the values of the constants c_{jn} that appear in Eq. (5.25).

$$\begin{aligned}
c_{00} &= +149775/302848 \\
c_{01} &= -114885/86528 \\
c_{02} &= -426765/86528 \\
c_{03} &= +466785/86528 \\
c_{04} &= +891135/86528
\end{aligned} \tag{B.6}$$

$$\begin{aligned}
c_{10} &= \sqrt{7} (-8665823/901502784) \\
& \quad - 1112932351/72120222720 \\
c_{11} &= \sqrt{7} (1152553/346731840) \\
& \quad - 1338324667/20605777920 \\
c_{12} &= \sqrt{7} (+244872559/4507513920) \\
& \quad - 1642544609/28848089088 \\
c_{13} &= \sqrt{7} (-146684593/4507513920) \\
& \quad + 30716745433/144240445440 \\
c_{14} &= \sqrt{7} (-2049139/26830440) \\
& \quad + 316758415/1373718528 \\
c_{20} &= \sqrt{7} (-78548959/534223872) \\
& \quad - 1853639/5136768 \\
c_{21} &= \sqrt{7} (+31249571/3205343232) \\
& \quad - 418846951/457906176 \\
c_{22} &= \sqrt{7} (+829392673/1068447744) \\
& \quad - 12997139/82188288 \\
c_{23} &= \sqrt{7} (-1358230247/3205343232) \\
& \quad + 9232063357/3205343232 \\
c_{24} &= \sqrt{7} (-19441831/21805056) \\
& \quad + 335959781/152635392
\end{aligned} \tag{B.7}$$

B.4 Formulas for the Parameters γ

There are six contributions γ to U_{field} that occur at order $1/\mu$. The following formulas [WMJ12] hold when the tensor Stark and Zeeman phases are each locked respectively to integer multiples k_ϵ and k_β of π , and in the case of γ_1 and γ_2 , when $\alpha_z = 0$.

$$\gamma_1 = \mathcal{G}_{1,1} = \begin{cases} 2x_o(-\tau) & \text{for } k_\epsilon + k_\beta \text{ even,} \\ 2x_e(-\tau) & \text{for } k_\epsilon + k_\beta \text{ odd,} \end{cases} \tag{B.9}$$

$$\gamma_2 = \mathcal{B}_{1,1} = \begin{cases} 0 & \text{for } k_\epsilon + k_\beta \text{ even,} \\ 2y_e(-\tau) & \text{for } k_\epsilon + k_\beta \text{ odd.} \end{cases} \tag{B.10}$$

$$\gamma_3/5 = \mathcal{B}_{2,1}^{(1)} = 2(-1)^{k_\beta} \int_{-\tau}^{\tau} x_e(t) y_e(t) \cos g(t) dt. \tag{B.11}$$

$$\gamma_4/5 = \mathcal{B}_{2,1}^{(2)} = -2(-1)^{k_\beta} \int_{-\tau}^{\tau} x_o(t) x_e(t) \sin g(t) dt. \quad (\text{B.12})$$

$$\gamma_5/5 = \mathcal{G}_{2,1}^{(2)} = 2(-1)^{k_\beta} \int_{-\tau}^{\tau} \left\{ [x_e^2(t) + x_o^2(t) - y_e^2(t)] \cos g(t) + 2x_o(t) y_e(t) \sin g(t) \right\} dt, \quad (\text{B.13})$$

$$\gamma_6 = \mathcal{G}_{2,1}^{(1)} = \int_{-\tau}^{\tau} \{x_e^2(t) + x_o^2(t) + y_e^2(t)\} dt, \quad (\text{B.14})$$

In Eqs. (B.12) and (B.13) the function g is defined by

$$g(t) = 2 \int_0^t \beta_z(t') dt', \quad (\text{B.15})$$

which is odd in time. When $\alpha_z \neq 0$ there are in general additional shifts; to first order in α_z we have for example

$$\gamma_1 \rightarrow \begin{cases} 2x_o + 2\alpha_z y_e & \text{if } k_\epsilon + k_\beta \text{ is even} \\ 2x_e & \text{if } k_\epsilon + k_\beta \text{ is odd,} \end{cases} \quad (\text{B.16})$$

and

$$\gamma_2 \rightarrow \begin{cases} -2\alpha_z x_e & \text{if } k_\epsilon + k_\beta \text{ is even} \\ 2y_e - 2\alpha_z x_o & \text{if } k_\epsilon + k_\beta \text{ is odd.} \end{cases} \quad (\text{B.17})$$

Adding two measurements of γ_2 , taken for opposite signs of the electric field, isolates the rotation α_z .

B.5 Values of the Survival Probabilities c_M

In Table B.1 is tabulated the the probability c_M that an atom initially in a state $7S_{1/2} |5M\rangle$ ends after multiple cycles of excitation and spontaneous emission in the dark $7S_{1/2} |55\rangle$ state when rung with a laser tuned to the level $7P_{j'}, F'$, that propagates in the z direction, and that is circularly polarized with positive helicity. In Table B.2 is tabulated the similar probability c_M that an atom in

the same initial state ends in the dark $7S_{1/2} |50\rangle$ state when the laser is linearly polarized with its axis of linear polarization parallel to the z axis. We may call these probabilities c_M the survival probabilities because they equal the probability (as a function of M) that an atom initially in a state $7S_{1/2} |5M\rangle$ remains (or survives) in the $F = 5$ ground-state hyperfine level after many cycles of excitation and spontaneous emission instead of transferring to some state in the $F = 4$ level. All the probabilities derive from the Clebsch-Gordon coefficients that control the various branching ratios for spontaneous decay and are simple fractions. The probabilities for the eight different lasers are displayed in Fig. B.1

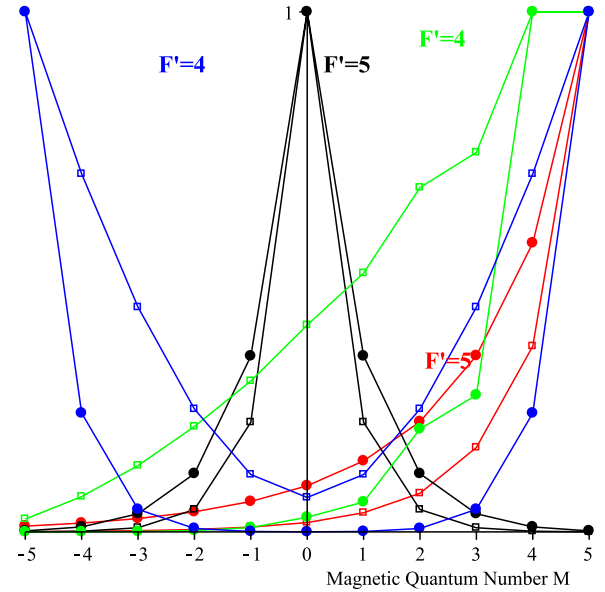


Figure B.1: The various survival probabilities for all of the eight patterns of single-laser excitation tabulated in Tables B.1–B.2. The four patterns of probabilities from using π light are symmetric about $M = 0$ and are shown with points in blue and black. The four patterns of probabilities from using σ^+ light are asymmetric about $M = 0$ and are shown with points in green and red. There are two patterns for each color, depending on whether P state involved has $j' = 1/2$ or $j' = 3/2$. The four patterns of probabilities (not shown) from using σ^- light are obtained by reflecting the patterns for σ^+ light about $M = 0$; there are 12 distinct patterns in all.

Table B.1: Probability of ending in $7S_{1/2}|55\rangle$ when starting in $7S_{1/2}|5M\rangle$ and pumping through the level $7P_{j'}$, F' with σ_+ light.

| M | $j' = 1/2$ $F' = 5$ | $j' = 3/2$ $F' = 5$ | $j' = 1/2$ $F' = 4$ | $j' = 3/2$ $F' = 4$ |
|-----|------------------------|------------------------|------------------------|----------------------------------------|
| 5 | 1 | 1 | 1 | 1 |
| 4 | 5 / 14 | 5 / 9 | 1 | 1 |
| 3 | 25 / 154 | 125 / 369 | 27 / 37 | 216 / 821 |
| 2 | 40 / 539 | 165 / 779 | 49 / 74 | 44016 / 222491 |
| 1 | 110 / 2989 | 70 / 513 | 847 / 1702 | 1139264 / 19801699 |
| 0 | 1179 / 65758 | 1864 / 21033 | 8799 / 22126 | 87686592 / 3108866743 |
| -1 | 55 / 5978 | 10 / 171 | 6419 / 22126 | 433345024 / 52850734631 |
| -2 | 9145 / 2005619 | 4865 / 126198 | 13447 / 66378 | 33742668288 / 13054131453857 |
| -3 | 98305 / 42117999 | 30695 / 1198881 | 132643 / 1039922 | 5403253438464 / 9307595726600041 |
| -4 | 32215 / 28078666 | 6755 / 399627 | 70623 / 1039922 | 211503496644608 / 2112824229938209307 |
| -5 | 110527 / 196550662 | 2107 / 189297 | 76825 / 3119766 | 834685333422080 / 90851441887343000201 |

Table B.2: Probability of ending in $7S_{1/2}|50\rangle$ when starting in $7S_{1/2}|5M\rangle$ and pumping through the level $7P_{j'}$, F' with π light.

| M | $j' = 1/2$ $F' = 5$ | $j' = 3/2$ $F' = 5$ | $j' = 1/2$ $F' = 4$ | $j' = 3/2$ $F' = 4$ |
|-----|------------------------|------------------------|------------------------|--------------------------|
| 5 | 7 / 57086 | 9 / 4732 | 1 | 1 |
| 4 | 35 / 28543 | 45 / 4732 | 55065 / 79994 | 8696678140 / 38083782007 |
| 3 | 455 / 57086 | 165 / 4732 | 17280 / 39997 | 1649572800 / 38083782007 |
| 2 | 1225 / 28543 | 265 / 2366 | 9450 / 39997 | 250270720 / 38083782007 |
| 1 | 12035 / 57086 | 400 / 1183 | 4410 / 39997 | 29102080 / 38083782007 |
| 0 | 1 | 1 | 2646 / 39997 | 4816896 / 38083782007 |
| -1 | 12035 / 57086 | 400 / 1183 | 4410 / 39997 | 29102080 / 38083782007 |
| -2 | 1225 / 28543 | 265 / 2366 | 9450 / 39997 | 250270720 / 38083782007 |
| -3 | 455 / 57086 | 165 / 4732 | 17280 / 39997 | 1649572800 / 38083782007 |
| -4 | 35 / 28543 | 45 / 4732 | 55065 / 79994 | 8696678140 / 38083782007 |
| -5 | 7 / 57086 | 9 / 4732 | 1 | 1 |

Appendix C

Discharge Current Systematics

C.1 Introduction

We will look at an experimental model for the magnetic field normal to the electric field plates due to small amounts of discharge current between the plates. Ideally the discharge current is normal to the plates, so the magnetic field in the normal direction is zero. Under realistic conditions, however, the discharge current may be at an angle to the normal, and thus generate a normal magnetic field. Comparison of data taken with the experimental model and the results from calculations will be made. The calculations will then be used to estimate the time-averaged normal magnetic field seen by the atoms in the EDM fountain as a function of discharge current.

This note compares data from an experimental model of the normal magnetic field, due to a discharge current between two electric field plates, with a calculation of the normal field that uses the Biot-Savart law. Rather than using high-voltage plates in a vacuum, we mock up the experimental situation with a low-voltage set of plates in air, and put a conducting short between the plates (Fig. C.1). The calculation is then used as a basis for a three dimensional Monte Carlo calculation of the time-integrated normal magnetic field seen by a set of atoms launched within a 5 mm distance of the transverse center of the plates. The field is due to a discharge current at an angle of 30 degrees from the plate normal, starting at a random position on one plate. The position of the discharge is moved parallel to the plane of the plates, both in the transverse and longitudinal directions.

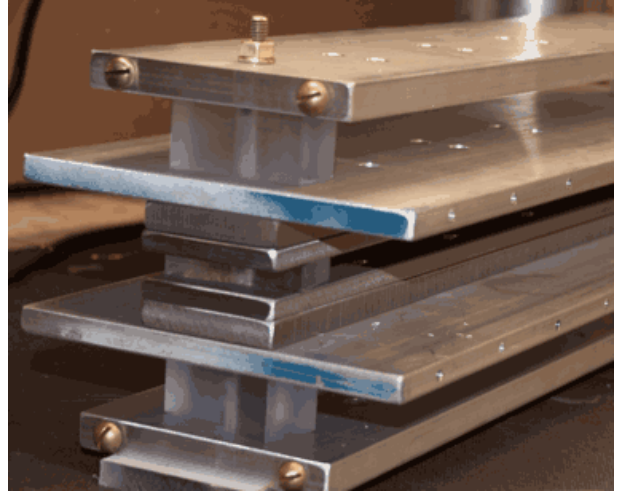


Figure C.1: Model electric field plates built to resemble those in Fig. 4.6

C.2 Experimental Model Geometry

The geometry of the experimental model is shown below.

In addition to the holes that allow the magnetic probe to be placed near the short, each Al plate has holes around the perimeter (labeled 1–9 on the bottom plate in Figure C.2) to allow the insertion of current leads. We operate the model by attaching current leads to the top and bottom Al plates and inserting a short at an arbitrary location near the center of the model.

We apply approximately 2 volts between the leads, giving us a current of about 1.5 amps. We then insert the magnetic probe in the holes and measure

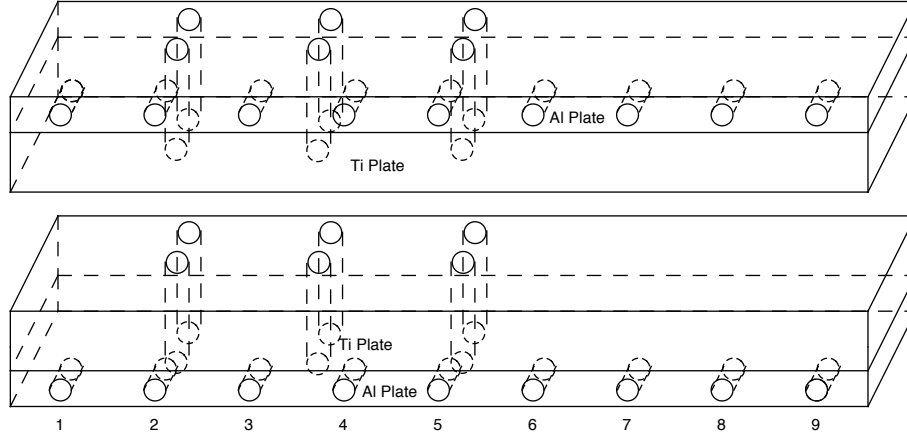


Figure C.2: The model plates are shown. The backing plates are made of Al, the inner plates are made of Ti, and there are 6 holes to insert a cylindrical magnetic probe which measures the B field normal to the plates. The width of the plates is 2 inches, the length 18 inches, and the Ti thickness is $5/8''$, while the Al thickness is $3/8''$. The plates are separated by 1 cm (not to scale).

the field. Since we only have measurement holes on one longitudinal half of the model, we simulate the other half by placing the current leads on the opposite side of the model. For instance, we initially insert the current leads in hole #1 on both the top and bottom plates, and measure the field in all six positions. We then insert the current leads in hole #9 on each plate, and remeasure the field. This allows us to simulate a rough experimental field map over the entire apparatus.

C.3 General Calculation

We start with the Biot-Savart law for a closed magnetic circuit,

$$B = \frac{\mu_o}{4\pi} \oint \frac{I d\vec{l} \times \vec{r}}{|\vec{r}|^3}. \quad (\text{C.1})$$

We then sum the circuit due to four line currents to make up our current loop, writing

$$B = \sum_{i=1}^4 \int d\vec{B}_i, \quad (\text{C.2})$$

where

$$d\vec{B}_i = \frac{\mu_o}{4\pi} \frac{I d\vec{l}_i \times \vec{r}}{|\vec{r}|^3} \quad (\text{C.3})$$

for each of the line currents along $d\vec{l}_i$. The field is evaluated at each point of interest (x, y, z) , where the vector \vec{r} is the vector between each point on the line segment and the point of interest. The current loop is nominally at a distance $d/2$ from the x axis, and the lengths of the segments are a and b , as shown in Figure C.3.

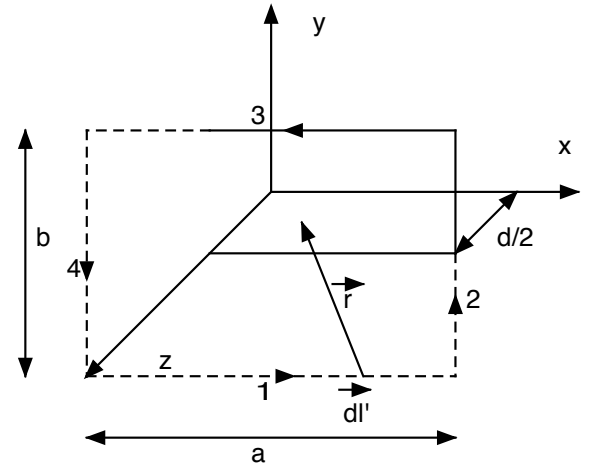


Figure C.3: The current loop is shown. We sum over each of the 4 segments, integrating over dl' for each segment, and calculate the magnetic field at position r .

For this calculation (note this coordinate system uses x as the direction of the beam and y as the

direction normal to the electric field plates) we are only interested in the normal component of the magnetic field, B_y , since a field in that direction which reverses with the voltage mimics an EDM.

To mock up the angle of the discharge we allow segment 2 of the current loop to be at an angle θ_2 to the x axis, and in the x - z plane. We assume that the segment is centered at $d/2$, and the upper (positive y) end of the segment moves in the $-z$ direction, while the bottom (negative y) end of the segments moves in the $+z$ direction.

The motion of segment 2 also moves the connections with segments 1 and 3. We account for this by keeping their connection points with segment 4 fixed, while allowing their endpoints with segment 2 to move by the same amount as the endpoints of segment 2. Note that the length of all three segments (1, 2, and 3) changes when we change the angle of segment 2, since segment 2 must still reach the upper and lower plates, and segments 1 and 3 must still connect to segment 2, which has moved transversely to the longitudinal axis of the plates.

The calculation also allows the location of segment 2 in the x - z plane to move. We can pick a value of $d_0/2$ to initially set the z location of the circuit, and allow segment 2 to move to a z position of $d_2/2$.

As an example, for segment 2 we have

$$\vec{dl}_2 = \hat{j} dl_2 \cos \theta_2 - \hat{k} dl_2 \sin \theta_2 \quad (C.4)$$

and

$$\vec{r} = (x - a/2)\hat{i} + (y - l_2 \cos \theta_2)\hat{j} + (z - d/2 + l_2 \sin \theta_2)\hat{k}. \quad (C.5)$$

Then, the cross product is given by

$$\vec{dl}_2 \times \vec{r} = \begin{vmatrix} \hat{i} & \hat{j} & \hat{k} \\ 0 & dl_2 \cos \theta_2 & -dl_2 \sin \theta_2 \\ x - a/2 & y - l \cos \theta_2 & z - d/2 + l \sin \theta_2 \end{vmatrix} \quad (C.6)$$

We are only interested in the normal component of the magnetic field, which is

$$[\hat{j} \cdot (\vec{dl}_2 \times \vec{r})]\hat{j} = (x - a/2)(-dl_2 \sin \theta_2). \quad (C.7)$$

We can calculate the square of the distance to the point of interest, which is

$$r^2 = l^2 - 2l\beta_2 + \alpha_2, \quad (C.8)$$

where

$$\alpha_2 = x^2 + y^2 + z^2 - ax - zd + \frac{a^2 + d^2}{4} \quad (C.9)$$

and

$$\beta_2 = y \cos \theta_2 - (z - d/2) \sin \theta_2. \quad (C.10)$$

Therefore we now have

$$dB_2 \hat{j} = \frac{\mu_o I}{4\pi} \frac{(-x + a/2) \sin \theta_2 dl}{[l^2 - 2l\beta_2 + \alpha_2]^{3/2}} \hat{j}. \quad (C.11)$$

We then integrate and find

$$\begin{aligned} B_2 \hat{j} &= \int_{-b/(2 \cos \theta_2)}^{b/(2 \cos \theta_2)} dB_2 \hat{j} \\ &= \frac{\mu_o I}{4\pi} (-x + a/2) \sin \theta_2 \\ &\quad \times G[\alpha_2, \beta_2, b/(2 \cos \theta_2)] \hat{j}, \end{aligned} \quad (C.12)$$

where

$$G[\alpha, \beta, c] = g[\alpha, \beta, c] - g[\alpha, \beta, -c] \quad (C.13)$$

and

$$g[\alpha, \beta, c] = \frac{c - \beta}{(\alpha - \beta^2) \sqrt{c^2 - 2\beta c + \alpha}}. \quad (C.14)$$

We calculate similar integrals for the normal components of B due to segments 1, 3, and 4 and add them to get the final normal field. In the case of segments 1 and 3 we also move the end of the segment connecting to segment 2 to the appropriate location so that it makes a complete circuit, as described above.

Similarly, we can make an equivalent calculation for a short that is angled in the longitudinal direction. In the next section we present the results of both calculations compared to the data taken with the model.

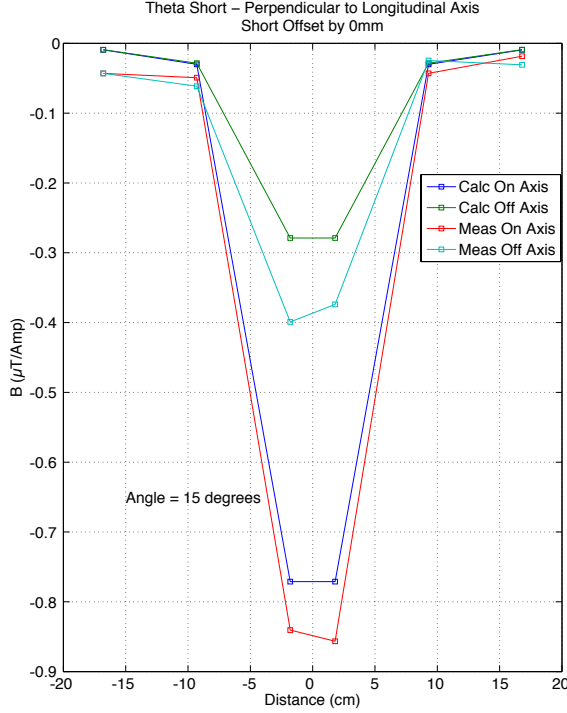


Figure C.4: Comparison of the calculated normal field and the measured normal field for a transverse short at an angle of ~ 15 degrees. Measurements and calculations are made at locations both on the longitudinal axis and displaced from the longitudinal axis by 1.8 cm.

C.4 Comparison of Model to Calculation

The first comparison is for the case where the short is angled in the direction transverse to the longitudinal axis of the plates.

Figure C.4 shows four curves for the normal field with a transverse short. The red and blue curves are what is measured and calculated for positions on the longitudinal axis of the plates, while the green and turquoise curves are for positions displaced from the longitudinal axis by 1.8 cm.

The next comparison is for the case where the short is angled in the direction parallel to the longitudinal axis of the plates. Figure C.5 shows four curves for the normal field with a longitudinal short. The red and blue curves are what is measured and calcu-

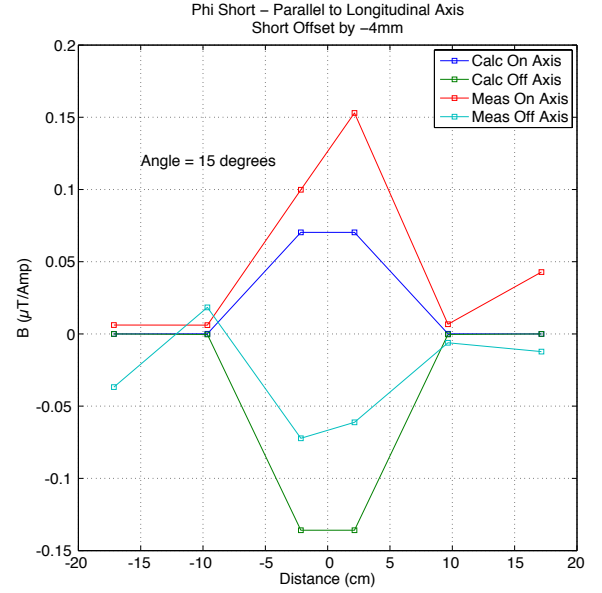


Figure C.5: Comparison of the calculated normal field and the measured normal field for a longitudinal short at an angle of ~ 15 degrees. Measurements and calculations are made for points on the longitudinal axis and displaced from the longitudinal axis by 1.8 cm.

lated for positions on the longitudinal axis of the plates, while the green and turquoise curves are for positions displaced from the longitudinal axis by 1.8 cm. Since there would be no normal field on the longitudinal axis if the short were also on the axis, the short has been displaced from the axis by ~ 4 mm. In both the transverse and longitudinal cases the measurements and the calculations agree to a factor of two, or better. For the longitudinal case the measurements are extremely sensitive to the exact displacement of the short from the longitudinal axis, which helps to explain the discrepancy. The case with the transverse short is less sensitive to this displacement, and the agreement is also better.

Since the normal field for the transverse case is significantly larger than the normal field for the longitudinal case, we will use the transverse case as a model to calculate the time-integrated normal field seen by the atoms in the fountain.

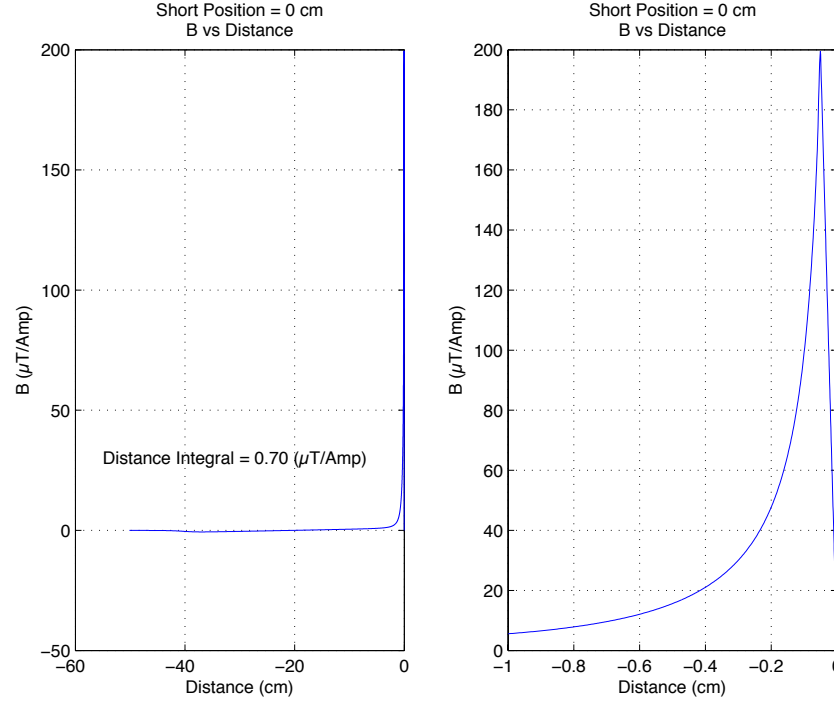


Figure C.6: The graph on the left shows the field per unit current for a discharge at a 30 degree angle transverse to the longitudinal axis. The graph on the right is a blowup in the region of the discharge. The discharge radius is 5 mm in this example, and is located on the longitudinal axis at the top of the fountain.

C.5 Time-Averaged Field Seen by the Fountain Atoms

The field will be calculated for the case of a transverse short at an angle of 30 degrees. The current in the short is a strong function of the electric field, and the field is reduced proportional to the inverse of the cosine of the angle. The 30 degree angle is chosen since it reduces the field to 87% of its original value, which should reduce the discharge current substantially.

The magnetic field is strongest close to the discharge. The atoms in the fountain are going slowest at the top of the fountain, where they turn around. Figure C.6 shows the magnetic field as a function of distance, over the entire plate length, and in detail over the area nearest the discharge. The discharge is assumed to be located at the top of the fountain, and to have a radius of 0.5 mm. The field is calculated inside the discharge by assuming a constant current density inside the discharge.

The distance-average of the normal magnetic field is calculated by integrating the field over the left-hand graph in Figure C.6 and dividing by the total distance. The result of $0.7 \mu\text{T}/\text{A}$ is shown in the figure.

We are actually interested in the time-average of the normal magnetic field over the trajectory of the atoms. Figure C.7 shows the normal magnetic field for the above case as seen by the atoms which turn around at the center of the discharge. It also indicates that the time-average of the normal magnetic field is $7.0 \mu\text{T}/\text{A}$. Note that the atoms travel through the field twice, once on the way up and once on the way down.

C.6 Monte Carlo Calculation

The final step is to calculate the time-averaged field for a large number of different locations of the dis-

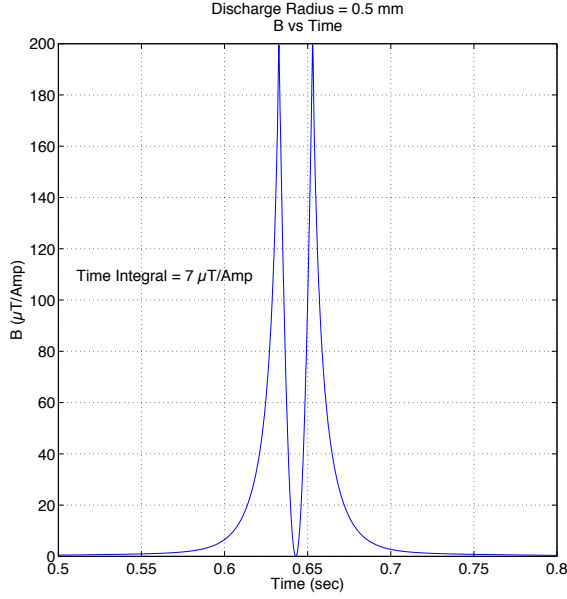


Figure C.7: The graph shows the field per unit current for a discharge at a 30 degree angle transverse to the longitudinal axis, as a function of time as seen by the atoms moving up and down in the fountain. The discharge radius is 5 mm in this example, and is located on the longitudinal axis at the top of the fountain.

charge. We allow the discharge to be anywhere between the plates, using a random number generator to vary the transverse position from -2.5 cm to $+2.5$ cm from the axis, and vary the longitudinal position along a 40 cm section of the plates. The maximum height of the discharge is at the point where the atoms reverse their trajectories.

Next, since each atom is not launched from exactly the same transverse position, we have looked at two cases. In the first case, the transverse launch position varies from -5 mm to $+5$ mm (or $\sim 2\sigma$) off the longitudinal axis of the plates with a random distribution. In the second case a more realistic calculation was performed, with the atom's transverse position represented by a Gaussian distribution centered on the axis with a standard deviation $\sigma = 2.5$ mm. This is a reasonable approximation of the optics solution for our fountain.

Finally, for a number of cases the radius of the discharge was varied between 0.1 mm and 0.5 mm. For an atom that passes through the discharge, the in-

tegrated field will be stronger if the discharge radius is smaller. However, this only affects atoms that have their distance from the center of the discharge location less than the discharge radius, and thus rarely made a difference in the outcome of the calculation.

One can see this by calculating the area of the discharge of a given radius, for instance $A_d = \pi \times (0.1 \text{ mm})^2 = 0.0314 \text{ mm}^2$, and comparing that to the area of the plates where the discharge can randomly occur, $A_p = 50 \times 400 \text{ mm}^2 = 2 \times 10^4 \text{ mm}^2$. Thus, the discharge radius will have an effect on only a fraction A_d/A_p of the cases, or about 1 case in 640,000.

Table C.1 shows the results of a number of Monte Carlo calculations.

Table C.1: Monte Carlo Calculations

| Disch. rad. (mm) | Num. lon. pos. | Num. trans. pos. | Num. atom pos. | Atom Dist. | Av. field int. |
|------------------|----------------|------------------|----------------|------------|----------------|
| 0.5 | 100 | 100 | 1 | Rand | -0.0273 |
| 0.5 | 30 | 30 | 1 | Rand | -0.0244 |
| 0.5 | 5 | 5 | 2 | Rand | -0.0290 |
| 0.5 | 20 | 20 | 20 | Rand | +0.0200 |
| 0.5 | 10 | 10 | 100 | Rand | +0.0111 |
| 0.1 | 20 | 20 | 20 | Gauss | +0.0002 |
| 0.5 | 20 | 20 | 20 | Gauss | +0.0056 |
| 0.1 | 20 | 20 | 20 | Gauss | +0.0060 |

If we average over all of the cases with the random distribution of the atoms, we get an overall average normal magnetic field integral of $-0.0009 \mu\text{T}/\text{A}$. Taking the 3 cases with the Gaussian distribution, the average is equal to $0.0039 \mu\text{T}/\text{A}$.

Thus, a reasonable upper limit for the average normal magnetic field due to random discharge currents would be $0.005 \mu\text{T}/\text{A}$.

Appendix D

Relative Systematic Effect by Atom, Isotope, and State

D.1 Variation with Tensor Polarizability

We wish to examine, relative to ^{211}Fr ($F = 5$), the sensitivity to motional systematic effects in ^{85}Rb ($F = 3$), ^{87}Rb ($F = 2$), ^{133}Cs ($F = 4$), and ^{221}Fr ($F = 3$). In the expansion order that generates the systematic terms to which the experiment is sensitive, that sensitivity varies inversely with the square of the tensor polarizability. Systematic terms also vary with F , the total angular momentum and with M , the z projection of the angular momentum, with different systematic terms having different dependences on F and M . All however have the same inverse square dependence on the tensor polarizability. In Table D.1 we show the tensor polarizabilities of the different atomic isotopes and the inverse square of the tensor polarizability relative to ^{211}Fr .

Table D.1: Ground State Tensor Polarizabilities

| Isotope | Tensor Polarizability α_F^T (J/(V/m) ²) | $(1/\alpha_F^T)^2$ relative to ^{211}Fr |
|-------------------|------------------------------------------------------------------|--------------------------------------------------------|
| ^{211}Fr | 1.1×10^{-44} | 1 |
| ^{221}Fr | 3.4×10^{-45} | 1.0×10^1 |
| ^{133}Cs | 2.2×10^{-45} | 2.0×10^1 |
| ^{87}Rb | 9.3×10^{-46} | 1.4×10^2 |
| ^{85}Rb | 3.0×10^{-46} | 1.3×10^3 |

D.2 Variation With Angular Momentum

To extract the dependence on total angular momentum, we assume that the same electric field E , transit time T , and the same residual magnetic fields and magnetic field gradients are present, the same (basic) state preparation and analysis scheme is used, and that we examine the superposition of states: $|\Phi_0\rangle = \frac{1}{\sqrt{2}}(|F, M\rangle + |F, -M\rangle)$.

The equations for the observable signal (\mathcal{P}^o) that changes sign upon reversal of the electric field are given for $F = 5, 4$, and 3 by Wundt, Munger and Jentschura [WMJ12]. For $F = 5$ we have

$$\begin{aligned} \mathcal{P}^o \left(\theta, |\Phi_0\rangle = \frac{1}{\sqrt{2}}(|5, 5\rangle + |5, -5\rangle) \right) = \\ \sin(10\theta) \left(5D - \frac{5\mathcal{B}_{2,2}^{(1,o)}}{162\mu^2} \right) \frac{1}{128} (210c_1 + 45c_3 + c_5 - 126c_0 - 120c_2 - 10c_4) \\ + \frac{5}{7} \frac{1}{512} \frac{\mathcal{B}_{2,2}^{(2)}}{\mu^2} \left(2 \sin(5\theta) \cos(3\theta) [7c_0 - 4c_2 - 3c_4] + \sin(3\theta) \cos(5\theta) [13c_3 + c_5 - 14c_1] \right) \\ + \mathcal{O}(\mu^{-4}) . \end{aligned} \quad (\text{D.1})$$

Table D.2: Table of Symbols

| Symbol | Quantity |
|-----------------------------|---------------------------------------------------------------------------------------------------------------------------------------------------------------|
| θ | analysis laser polarization angle relative to preparation polarization |
| D | $D = d_e R E_z T / (\hbar F)$, electron EDM signal |
| $\mathcal{B}_{2,2}^{(1,o)}$ | magnetic fields and gradients related to geometric phase effect |
| μ | perturbation expansion term |
| c_M | probability that an atom initially in the state $ F = I + \frac{1}{2}, M\rangle$ remains in the level $F = I + \frac{1}{2}$ after being fluoresced by a laser |
| $\mathcal{B}_{2,2}^{(2)}$ | magnetic fields related to eigenvalue shift |
| T | transit time in the electric field |
| d_e | electron EDM |
| R | EDM enhancement factor |
| E_z | electric field |
| α_F^T | tensor polarizability |

The coefficients c_M , for $M = -M, \dots, F$, are the probabilities that an atom initially in a state $|F, M\rangle = |I + 1/2, M\rangle$ would after state analysis remain in the upper ($F = I + 1/2$) hyperfine level. The set of coefficients c_M varies with the frequency and polarization of the laser doing the optical pumping; for $F = 5$ and for pumping with circular and with linearly polarized light the sets of coefficients are tabulated as exact fractions in Table B.1 and in Table B.2, respectively. (The exact coefficients for $F = 4$, suitable for cesium, are given in Table I of Wundt, Munger, and Jentschura¹ [WMJ12].) For analysis using linearly polarized light making transitions to the $P_{3/2}$ state, we have

$$\frac{1}{128} (210c_1 + 45c_3 + c_5 - 126c_0 - 120c_2 - 10c_4) = -37571/75712 \approx -0.496 . \quad (\text{D.2})$$

For different laser frequency and polarization the expression on the left will still be of order unity, because c_M being a probability we have $0 \leq c_M \leq 1$. In all cases there is no dependence on the tensor polarizability.

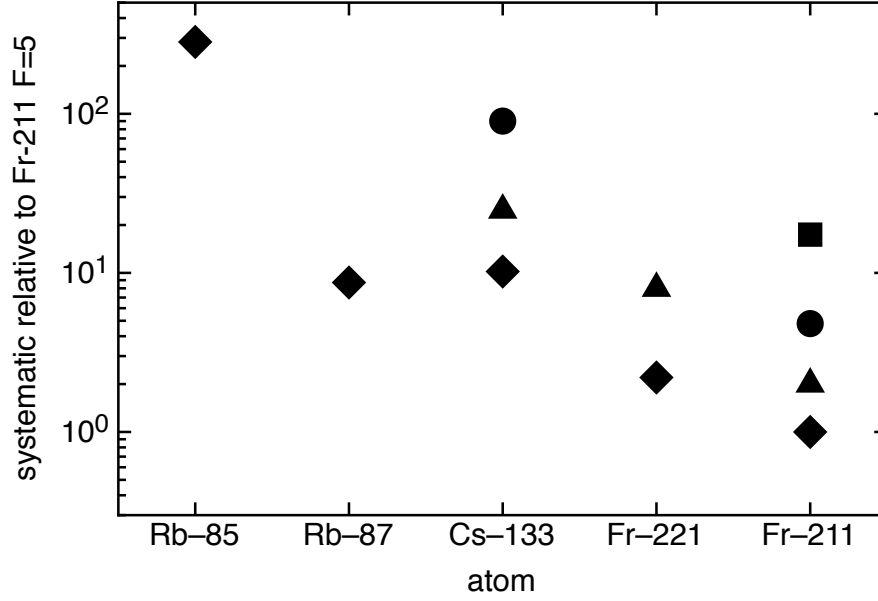


Figure D.1: Relative $\mathcal{B}^{(1,o)}$ motional systematic effects (related to geometric phase effect) for ^{85}Rb ($F = 3$), ^{87}Rb ($F = 2$), Cs ($F = 4$), and ^{221}Fr ($F = 3$) relative to ^{211}Fr ($F = 5$). All are for a superposition of states $|\Phi_0\rangle = \frac{1}{\sqrt{2}}(|F, M\rangle + |F, -M\rangle)$ where the diamonds are for $|M| = F$, triangles for $|M| = F - 1$, circles for $|M| = F - 2$, and the square for $|M| = F - 3$. Most of the difference in sensitivity arises because of the differences in tensor polarizability.

The $\mathcal{B}_{2,2}^{(1,o)}$ term

We look at the part involving the $\mathcal{B}_{2,2}^{(1,o)}$ term, which is the dominant systematic once the atoms are in the full electric field. From comparison with the terms for the superposition of $\frac{1}{\sqrt{2}}(|F, M\rangle + |F, -M\rangle)$ (See Eq. 3.43, 3.44, 5.1, 5.2, and Eq. I1–I4 in appendix I of Wundt, Munger and Jentschura [WMJ12]) we have that the term involving D and $\mathcal{B}_{2,2}^{(1,o)}$ can be reproduced by

$$M D - \frac{M}{2} \frac{(2F+1)^2 \mathcal{B}_{2,2}^{(1,o)}}{(2M-1)^2 (2M+1)^2 \mu^2}, \quad (\text{D.3})$$

where the factor of M in the product $M D$ completes the term for the EDM.

From $\mu = \epsilon_z^2(t)$ and for $\epsilon_z(t)$, E_S , and A_S the definitions

$$\epsilon_z = \frac{E_z(t)}{E_S}, \quad E_S = \sqrt{\frac{\hbar}{T A_S}}, \quad \text{and} \quad A_S = -\frac{3 \alpha_F^T}{2F(2F-1)}, \quad (\text{D.4})$$

we get²

¹In that paper the symbol p_M is used instead of c_M .

²For the Stark effect contribution to the energy splitting:

$$\mathcal{E}_S = -\frac{1}{2} \alpha_{FM} E_z^2, \quad \text{with} \quad \alpha_{FM} = \alpha_F^S + \frac{3F_z^2 - F(F+1)}{F(2F-1)} \alpha_F^T,$$

where all dependence on the magnetic quantum number M is explicit in the form of the operator F_z , Wundt et al. [WMJ12] state “The parts of ... α_{FM} that are independent of F contribute to a global shift of the whole hyperfine manifold and so

$$\mu^2 = \left(\frac{3TE_Z^2\alpha_F^T}{2F(2F-1)\hbar} \right)^2 \quad (\text{D.5})$$

Combining with Eq. D.3 gives

$$MD - \frac{M}{2} \frac{(2F-1)^2(2F+1)^2}{(2M-1)^2(2M+1)^2} \frac{F^2}{(3\alpha_F^T E_Z^2 T)^2} \mathcal{B}_{2,2}^{(1,o)}. \quad (\text{D.6})$$

From Eq. D.6 and Figure D.1 we note:

- Atoms with smaller nuclear spin are *less* sensitive to the $\mathcal{B}_{2,2}^{(1,o)}$ term. However nature has arranged that alkali atoms with small nuclear spin also have small tensor polarizability, α_F^T . Thus the very heavy high spin isotopes have in the end smaller systematic effects.
- This systematic for a ^{221}Fr experiment is only a factor of two worse than for ^{211}Fr experiment. However the world's known supply of ^{229}Th is not sufficient to rival the francium intensities at TRIUMF.
- For an EDM null experiment, the systematic sensitivity to the $\mathcal{B}_{2,2}^{(1,o)}$ term of Cs $|\Phi_0\rangle = \frac{1}{\sqrt{2}}(|4,4\rangle + |4,-4\rangle)$ is almost identical to that of ^{87}Rb $|\Phi_0\rangle = \frac{1}{\sqrt{2}}(|2,2\rangle + |2,-2\rangle)$. EDM sensitivity for Cesium ($R = 117$) however is larger than for ^{87}Rb ($R = 25$). This would give ^{87}Rb a slight edge for a null experiment, but see the next item.
- For an EDM null experiment, compared to ^{87}Rb $|\Phi_0\rangle = \frac{1}{\sqrt{2}}(|2,2\rangle + |2,-2\rangle)$ or Cs $|\Phi_0\rangle = \frac{1}{\sqrt{2}}(|4,4\rangle + |4,-4\rangle)$, the systematic sensitivity to the $\mathcal{B}_{2,2}^{(1,o)}$ term of Cs $|\Phi_0\rangle = \frac{1}{\sqrt{2}}(|4,3\rangle + |4,-3\rangle)$ and $|\Phi_0\rangle = \frac{1}{\sqrt{2}}(|4,2\rangle + |4,-2\rangle)$ is 2.5 times and 9 times larger respectively. And because the sensitivity to the EDM scales as M/F , the effective enhancement factors for these Cs states are $R = 88$ and $R = 59$ respectively. There being in Cs, three different sets of superpositions of $\pm M$ with different systematic sensitivities that can be used either individually or also in combination versus one in ^{87}Rb , would seem to make Cs the more attractive candidate for an EDM null experiment.

introduce no change in the atomic state other than a global phase.” The terms in α_F^S and in $F(F+1)\alpha_F^T/F(2F-1)$ are accordingly dropped in writing the effective Hamiltonian for the $(F = I + 1/2)$ manifold:

$$H_t = A_S F_z^2 E_z^2 + \mu_B g_F \vec{F} \cdot \vec{B} - (R d_e/F) F_z E_z.$$